

Revisiting predictions for cosmic-ray antinucleon fluxes from Galactic Dark Matter

Lorenzo Stefanuto,^{1,2,*} Mattia Di Mauro,^{2,†} Fiorenza Donato,^{1,2,3,‡}

Nicolao Fornengo,^{1,2,§} Jordan Koechler,^{2,¶} and David Maurin^{4,**}

¹*Dipartimento di Fisica, Università di Torino, via P. Giuria, 1, 10125 Torino, Italy*

²*Istituto Nazionale di Fisica Nucleare, Sezione di Torino, Via P. Giuria 1, 10125 Torino, Italy*

³*Theoretical Physics Department, CERN, 1211 Geneva 23, Switzerland*

⁴*LPSC, Université Grenoble-Alpes, CNRS/IN2P3, 38026, Grenoble, France*

The data on cosmic antiprotons have reached an outstanding precision on energies spanning from GeV to hundreds of TeV, thanks to the space-based AMS-02 experiment. The balloon-borne GAPS experiment, which just completed its first Antarctic flight, will address antiproton and antideuteron fluxes well below GeV energies. Antinuclei in cosmic rays, as well as being produced by spallation reactions between cosmic-ray nuclei and the atoms of the interstellar medium, may hide contributions from exotic sources, such as particle dark matter annihilation in the Galaxy. In this paper, we present predictions for cosmic antiproton, antideuteron and antihelium fluxes both from secondary and dark matter origin. We use state-of-the-art production spectra, nuclear coalescence for antinuclei, and Galactic propagation models to derive upper limits on the dark matter annihilation cross-section from AMS-02 antiproton data in different propagation scenarios (BIG and QUANT). We quantify the impact of future GAPS data, showing that its sensitivity to sub-GV antiprotons could improve the $\langle\sigma v\rangle$ constraints by up to an order of magnitude for light DM ($m_\chi \lesssim 50$ GeV). For heavier antinuclei, the detection perspective with existing and upcoming experiments are derived for those scenarios consistent with AMS-02 antiproton flux. The detectability of such signals strongly depends on the experiment, the propagation model, and the hadronization tuning. Our analysis underscores the complementarity of antinuclei channels for indirect DM searches and the critical role of low-energy windows in constraining light DM candidates.

I. INTRODUCTION

The search for antimatter in space has reached the status of precision physics with the data on positrons and antiprotons collected firstly by the PAMELA satellite-borne experiment [1–4] and currently by AMS-02 on board the International Space Station [5–7]. As for antinuclei, no detection has been established so far [4, 7–11]. The strongest upper bound on the antideuteron flux has been fixed by the BESS-Polar II experiment [11] at $6.7 \times 10^{-5} (\text{m}^2 \text{sr GeV}/n)^{-1}$ in the range of kinetic energies per nucleon $E_{k/n} \in [0.163, 1.100]$ GeV/ n . It is however expected that AMS-02 could reach a sensitivity of $2\text{--}8 \times 10^{-7} (\text{m}^2 \text{sr GeV}/n)^{-1}$ in the range $E_{k/n} \in [0.2, 4]$ GeV/ n by about 2030 [12, 13]. The GAPS program [9, 10, 14] is designed to reach peak sensitivity comparable to AMS-02 in the low-energy window $E_{k/n} \in [0.1, 1]$ GeV/ n [14, 15]. The balloon-borne GAPS experiment has just completed its first successful flight (25 days) around Antarctica [16], and two more flights are foreseen in the next years.

The interest in cosmic-ray (CR) antinuclei is many-fold. Firstly, antiprotons are expected to be produced by spallation reactions of CR nuclei (mainly protons and

helium) on the interstellar medium (ISM) atoms, the so-called secondary component. The detection of a flux of antiprotons from 1 GeV to beyond 400 GeV probes that antimatter is produced in the Galaxy by inelastic scatterings of CR nuclei off proton and helium in the ISM, at a rate compatible with measured hadronic cross-sections [17–20]. Secondly, CR light antinuclei, especially antideuterons ($\bar{\text{D}}$) [21] and antihelium (${}^3\bar{\text{He}}$) [22, 23], are considered among the cleanest messengers for indirect dark matter (DM) searches. The reason resides in the baryon-number conservation, which implies a strong suppression of the secondary flux at kinetic energy per nucleon $E_{k/n} \lesssim 1$ GeV/ n [21, 24]. DM annihilation or decay in the Galactic halo, being non-baryonic particles, can annihilate into very low-energy antinuclei. Fluxes for the $\bar{\text{D}}$ flux from standard Weakly Annihilating Massive Particles (WIMPs) are typically predicted two orders of magnitude higher than the secondary production expectations at low $E_{k/n}$ [21, 25–29].

In this paper, we compute the CR antiproton and antideuteron fluxes both for the secondary component and for DM annihilation with the USINE propagation code [30]. Firstly, we compute primary \bar{p} fluxes including new source spectra, deriving updated bounds on the DM annihilation cross-section $\langle\sigma v\rangle$ by fitting AMS-02 data. We also quantify the effect that \bar{p} simulated GAPS data could have on the upper bounds of $\langle\sigma v\rangle$. Secondly, the differential production cross-sections for the secondaries and source spectra for primaries are calculated from Refs. [31, 32], where coalescence uncertainties are estimated to be 20% smaller than in previous modelings. In light of these results, we revisit the production of CR

* lorenzo.stefanuto@unito.it

† dimauro.mattia@gmail.com

‡ fiorenza.donato@unito.it

§ nicolao.fornengo@unito.it

¶ jordan.koechler@gmail.com

** dmaurin@lpsc.in2p3.fr

antinuclei in the Galaxy and explore the detection potential of \bar{D} and ${}^3\bar{\text{He}}$ with current and future experiments.

II. COALESCENCE MODELS

The production of light (anti)nuclei is commonly modeled via the *coalescence* of (anti)nucleons: a bound state forms when the relevant (anti)nucleons are sufficiently close in phase space. In phenomenological applications, this concept can be modeled in various ways, ranging from analytic prescriptions (useful for intuition and rapid estimates), to event-by-event afterburners interfaced with Monte Carlo (MC) generators, and ultimately to quantum-mechanical approaches based on Wigner functions. As most of the technical details and validation procedures are presented in Refs. [31, 32], we limit ourselves here to a concise summary of the implementations adopted in this work, highlighting the key assumptions and parameters.

A. Analytic (spherical) coalescence

The simplest approach assumes independent and isotropic emission of (anti)protons and (anti)neutrons, neglecting correlations in both momentum and configuration space [21, 26]. Coalescence is then encoded in a single momentum scale, the *coalescence momentum* p_{coal} . The invariant spectrum of a nucleus with mass number A and (Z, N) can be related to the corresponding single-(anti)nucleon spectra as

$$E_A \frac{d^3 N_A}{dp_A^3} = B_A \left(E_p \frac{d^3 N_p}{dp_p^3} \right)^Z \left(E_n \frac{d^3 N_n}{dp_n^3} \right)^N, \quad (1)$$

with the momenta evaluated at $p_{p,n} = p_A/A$. In practice one often sets $d^3 N_n/dp_n^3 \simeq d^3 N_p/dp_p^3$ (and similarly for antiparticles), so that for antideuterons one obtains

$$E_{\bar{D}} \frac{d^3 N_{\bar{D}}}{dp_{\bar{D}}^3} = B_2 \left(E_{\bar{p}} \frac{d^3 N_{\bar{p}}}{dp_{\bar{p}}^3} \right)^2. \quad (2)$$

In the spherical approximation B_A is proportional to p_{coal}^3 [21, 26]. Experimentally, coalescence factors extracted from collider data are typically $B_2 \sim \mathcal{O}(10^{-2}) \text{ GeV}^2/c^3$ in pp collisions around $p_T/A \sim 1 \text{ GeV}/c$, and often show an effective rise with p_T/A in multiplicity-integrated samples [33, 34]. Such trends can partly reflect genuine physics (e.g. changing emission volumes) and partly arise from spectral-shape effects when the proton and deuteron slopes are not self-similar [33, 35]. Because this framework ignores correlations, it is known to become unreliable precisely where correlations are strongest (e.g. at high transverse momentum or in boosted topologies [25, 31]). This motivates the use of event-by-event approaches.

B. Monte-Carlo coalescence with phase-space cutoffs

In MC afterburners, coalescence is applied directly to the event record and therefore automatically retains correlations generated by the underlying hadronization model [25, 31]. The most common prescription enforces a momentum-space proximity condition in the pair center-of-mass frame,

$$|\Delta\vec{p}| \equiv |\vec{p}_p - \vec{p}_n| < p_{\text{coal}}, \quad (3)$$

which we denote as the “ Δp model” [25–27, 36]. A minimal extension adds an explicit coordinate-space requirement [25],

$$|\Delta\vec{r}| \equiv |\vec{r}_p - \vec{r}_n| < r_{\text{coal}}, \quad (4)$$

with r_{coal} expected to be of the order of a few fm, comparable to the deuteron size [37]. We refer to this model as the “ $\Delta p + \Delta r$ model”. Besides capturing geometric information of the emitting source, the spatial cut is particularly useful to suppress coalescence between promptly produced antinucleons and antinucleons originating from displaced vertices (e.g., weak decays), since such pairs typically fail the Δr condition [38]. In both variants, the coalescence scale(s) are treated as effective parameters to be calibrated on collider measurements.

C. Wigner-function coalescence

A more microscopic formulation embeds coalescence into quantum mechanics by expressing the bound-state formation probability as an overlap in phase space between the two-particle density matrix of the \bar{p} - \bar{n} system and the density matrix of the deuteron bound state [39–44]. In Wigner language, the differential yield can be written schematically as

$$\frac{d^3 N_{\bar{D}}}{dp_{\bar{D}}^3} = S \int \frac{d^3 r d^3 q}{(2\pi)^3} \mathcal{D}(\vec{r}, \vec{q}) W_{\text{pn}} \left(\frac{\vec{p}_{\bar{D}}}{2} + \vec{q}, \frac{\vec{p}_{\bar{D}}}{2} - \vec{q}; \vec{r} \right), \quad (5)$$

where S accounts for spin/isospin statistics (for \bar{D} , $S = 3/8$), $\vec{r} \equiv \vec{r}_p - \vec{r}_n$ is the relative separation, and $\vec{q} \equiv (\vec{p}_p - \vec{p}_n)/2$ so that $\Delta\vec{p} = 2\vec{q}$. The kernel $\mathcal{D}(\vec{r}, \vec{q})$ is the deuteron Wigner function, fully determined by the bound-state wavefunction, while W_{pn} is the pair Wigner function encoding the correlated two-particle phase-space distribution provided by the event generator.

In practice, we estimate the momentum correlations directly from MC events and approximate the spatial part with a source model extracted from the same generator, following the strategy of Ref. [31]. A convenient working assumption is to factorize

$$W_{\text{pn}} \simeq H_{\text{pn}}(\vec{r}_p, \vec{r}_n) G_{\text{pn}}(\vec{p}_p, \vec{p}_n), \quad (6)$$

where G_{pn} is obtained from the two-particle momentum distribution in the event record (including correlations),

and H_{pn} encodes the effective space–time distribution of emission points. While this neglects genuine two-particle spatial correlations beyond those induced by the common event geometry, it makes the model transparent and allows controlled variations (e.g. different vertex prescriptions) to probe the corresponding uncertainty.

For an event-by-event implementation, Eq. (5) can be interpreted as defining an acceptance weight in $(\Delta\vec{r}, \Delta\vec{p})$ space. Concretely, for each \bar{p} – \bar{n} pair in an event we evaluate the kernel value $\mathcal{D}(\Delta r, \Delta p)$ (and the source factor, when needed), draw a random number $u \in [0, 1]$, and accept the pair to form an antideuteron if $u < \mathcal{W}(\Delta r, \Delta p)$, where \mathcal{W} is a suitably normalized weight. This is the same sampling logic adopted in Refs. [31, 32].

a. Gaussian kernel. As a compact benchmark we consider a Gaussian bound-state wavefunction, for which the Wigner kernel is analytic [27]. In this case the phase-space overlap effectively selects pairs with $\Delta r \lesssim \mathcal{O}(\text{few fm})$ and $\Delta p \lesssim \mathcal{O}(0.1\text{--}0.2 \text{ GeV})$, with the precise width controlled by a single momentum/length scale. The Gaussian implementation is flexible and numerically efficient, but it typically exhibits a degeneracy between the assumed source size and the bound-state scale; in practice this is broken by fixing the source size to a benchmark value (or by importing it from the generator), while tuning the remaining parameter to collider data, as done in Ref. [31] and in the present work.

b. Argonne kernel. To reduce the arbitrariness associated with purely phenomenological kernels, we also consider a Wigner kernel constructed from a realistic deuteron wavefunction based on the Argonne v_{18} nucleon–nucleon potential [45]. This wavefunction is constrained by scattering data and by the deuteron binding energy, and therefore provides a physically motivated reference without introducing an ad-hoc coalescence momentum. The corresponding Wigner kernel does not admit a simple closed form; we employ a tabulated representation as a function of (r, q) based on the parametrization in Ref. [46]. Once the underlying antinucleon production is fixed (through the MC tune), the Argonne/Wigner approach is comparatively predictive and serves as a useful cross-check of the calibrated phenomenological models [31].

Overall, these three classes of prescriptions (analytic, cutoff afterburners, and Wigner-based coalescence) allow us to: (i) connect to the standard literature, (ii) retain generator-level correlations relevant for collider and CR applications, and (iii) quantify the residual model dependence associated with the bound-state kernel and the effective source description.

III. PRODUCTION OF PRIMARY ANTINUCLEI FROM DARK MATTER ANNIHILATION

Primary antinuclei can be produced through DM annihilation in the Galactic halo. The corresponding pro-

duction rate of an antinucleus species i , per unit volume, time, and kinetic energy per nucleon $E_{k/n,i}$ (the so-called source term) can be written—assuming annihilation into a single channel—as:

$$q_i^{\text{prim}}(E_{k/n,i}, \vec{x}) = \frac{\langle\sigma v\rangle}{2\xi m_\chi^2} \rho_\chi^2(\vec{x}) \frac{dN_i}{dE_{k/n,i}}, \quad (7)$$

where $\langle\sigma v\rangle$ is the thermally averaged annihilation cross-section, m_χ is the DM particle mass, and $\xi = 1$ if DM particles are self-conjugate and 2 otherwise. The Galactic DM density distribution is described by ρ_χ . Following Refs. [20, 47], we adopt a spherically symmetric Navarro-Frenk-White (NFW) profile [48], with a scale radius $r_s = 19.6$ kpc [49], local DM density $\rho_\odot = 0.385 \text{ GeV/cm}^3$ [50], and solar distance $R_\odot = 8.20$ kpc [51]. Finally, $dN_i/dE_{k/n,i}$ denotes the differential yield of antinuclei at production for the specified DM annihilation channel.

To reliably predict the antinucleon differential yield, we employ a dedicated tuning of PYTHIA [52], an MC event generator for high-energy particle collisions. This tuning specifies hadronization parameters and branching ratios and is calibrated to reproduce key observables measured in e^+e^- collisions at the Z -pole, which provide a clean environment that closely resembles the hadronization conditions relevant for DM annihilation. The differential yields of \bar{D} and ${}^3\bar{\text{He}}$ are then obtained by applying the coalescence criteria described in Sect. II as an external afterburner to the PYTHIA events. Specifically, in order to form ${}^3\bar{\text{He}}$, the criteria must be valid for each of the three antinucleon pairs in the $\bar{p}\bar{p}\bar{n}$ configuration.

As an example, CosmiXs [31, 53, 54] provides predictions for \bar{p} and \bar{D} spectra from DM annihilation, relying on a calibrated PYTHIA setup that reproduces the \bar{D} multiplicity measured by the ALEPH [55] collaboration. It also accurately describes a range of meson and baryon observables from ALEPH and other e^+e^- experiments such as DELPHI, L3, and OPAL (see Refs. [56–58] for further details).

More recently, Ref. [38] extended this calibration to better predict the \bar{D} and ${}^3\bar{\text{He}}$ differential yields. In particular, the tuning was refined to reproduce the fragmentation fraction of b quarks into weakly decaying b -baryons, $f(b \rightarrow \Lambda_b) = 0.089 \pm 0.012$, as reported by the HFLAV collaboration [59], as well as the recent upper limit on the inclusive branching ratio $\text{BR}(\Lambda_b^0 \rightarrow {}^3\bar{\text{He}}X) < 6.3 \times 10^{-8}$ set by the LHCb experiment [60]. Accurately describing these observables is important, as the decay of weakly decaying B -hadrons constitutes a significant source of antinucleons, and hence of antinuclei. In the following, we refer to this setup as the “ Λ_b tuning”.

For primary antinuclei, the choice of coalescence model has a negligible impact on the predicted \bar{D} differential yield, $dN_{\bar{D}}/dE_{k/n,\bar{D}}$. As shown in Ref. [31], all considered coalescence models provide a good description of the \bar{D} multiplicity measured in e^+e^- collisions at the Z -pole by the ALEPH collaboration. The main limitation arises

Table I. Threshold kinetic energy per n of the primary CR projectile (p, He) to produce secondary antinuclei (\bar{p} , \bar{D} , ${}^3\bar{\text{He}}$) by colliding with nuclei from the ISM (H and He).

Process	$E_{k/n,c}^{\text{min}}$ [GeV/n]		
	secondary \bar{p}	secondary \bar{D}	secondary ${}^3\bar{\text{He}}$
p+H	$6 m_p$	$16 m_p$	$30 m_p$
p+He He+H	$3 m_p$	$7 m_p$	$12 m_p$
He+He	$1.125 m_p$	$2.5 m_p$	$4.125 m_p$

from the relatively large experimental uncertainty of this measurement, at the level of $\sim 30\%$. As a benchmark, we therefore adopt the Argonne Wigner model, which is among the most physically motivated approaches discussed in Sect. II.

IV. PRODUCTION OF SECONDARY ANTINUCLEI

Secondary antinuclei are produced through inelastic collisions between primary CRs and nuclei in the ISM. In principle, all CR species—from protons (p) and helium (He) up to heavier nuclei such as iron (Fe)—can contribute to secondary antinuclei production. However, CR species with charge $Z > 2$ are significantly less abundant, by at least two (one) orders of magnitude compared to protons (helium). Furthermore, the ISM is predominantly composed of hydrogen and helium. As a result, the dominant production channels for secondary antinuclei involve CR protons and helium nuclei colliding with hydrogen and helium targets.

The source term for secondary antinuclei of species i can be written as

$$q_i^{\text{sec}}(E_{k/n,i}, \vec{x}) = \sum_{c,t} \int_{E_{k/n,c}^{\text{min}}}^{\infty} dE_{k/n,c} 4\pi n_t(\vec{x}) \times \Phi_c(E_{k/n,c}, \vec{x}) \frac{d\sigma_{ct \rightarrow i}}{dE_{k/n,i}}(E_{k/n,c}), \quad (8)$$

where n_t denotes the number density of ISM target nuclei, $\Phi_c = v n_c$ is the interstellar flux of CR primaries, and $d\sigma_{ct \rightarrow i}/dE_{k/n,i}$ is the differential production cross-section for the secondary antinucleus i .

In Eq. (8), the lower integration limit $E_{k/n,c}^{\text{min}}$ represents the minimum kinetic energy per nucleon of the primary CR required to produce an antinucleus at rest, as dictated by baryon number conservation. Table I summarizes the corresponding threshold energies for different production channels and antinuclei species.

In Ref. [32], the differential production cross-section for antideuterons, $d\sigma_{pH \rightarrow \bar{D}}/dE_{k/n,\bar{D}}$, is derived using a dedicated tuning of PYTHIA, optimized to reproduce \bar{p} measurements in pp collisions. When combined with the coalescence models described in Sect. II, this tuning provides a good description of \bar{D} and ${}^3\bar{\text{He}}$ production as

measured by the ALICE experiment [33, 61]. Within this framework, the differential cross-section can be written as

$$\frac{d\sigma_{pH \rightarrow \bar{D}}}{dE_{k/n,\bar{D}}}(E_{k/n,p}) = \sigma_{pp}^{\text{inel}}(E_{k/n,p}) \frac{dN_{\bar{D}}}{dE_{k/n,\bar{D}}}(E_{k/n,p}), \quad (9)$$

where $\sigma_{pp}^{\text{inel}}$ is the total inelastic proton–proton cross-section (for which we adopt the parametrization of Ref. [62]), and $dN_{\bar{D}}/dE_{k/n,\bar{D}}$ denotes the antideuteron spectrum produced per collision, as obtained from the MC simulations.

This formulation can be generalized to arbitrary CR projectiles and ISM targets by parameterizing the total inelastic cross-section through an empirical mass-scaling relation [62]

$$\sigma_{ct}^{\text{inel}}(E_{k/n,c}) \simeq (A_c A_t)^{0.8} \sigma_{pp}^{\text{inel}}(E_{k/n,c}), \quad (10)$$

where A_c and A_t are the mass numbers of the CR projectile and the ISM target, respectively.

In this work, we compute the source term for secondary \bar{p} in Eq. (8) according to the results in [63] and already implemented in [18, 20]. The source term for secondary \bar{D} is computed as in Ref. [32], whose cross-sections are publicly available in the Zenodo repository [64]. As a benchmark, we adopt the results from the Gaussian Wigner coalescence model. In addition to being physically well motivated, this model provides the second-best fit to the ALICE \bar{D} data [32]. The best fit is achieved by the simple Δp model; however, as discussed in Ref. [32], this model is disfavored for applications to astrophysical \bar{D} production, since it may yield a non-negligible fraction of non-physical \bar{D} .

V. GALACTIC PROPAGATION AND SOLAR MODULATION

A. Transport equation and source terms

We consider the CRs diffusing in a cylindrical volume of radius $R_G = 20$ kpc and half-height L . The astrophysical sources and gas¹ are located in a thin disc of half-height $h = 100$ pc, where nuclear interactions and continuous energy losses and gains occur. The steady-state transport equation for the differential density n of Galactic CR antinuclei [65–67] in the thin disc approximation, assuming a constant velocity V_c perpendicular to the Galactic plane and isotropic and space-independent diffusion coefficient $K(E)$ as a function of total energy,

¹ We take the ISM density to be $n_{\text{ISM}} = 1 \text{ cm}^{-3}$ with 90% H and 10% He in number, and $\langle n_e \rangle = 0.033 \text{ cm}^{-3}$ and $T_e = 10^4 \text{ K}$.

reads [68]:

$$\begin{aligned}
& - \left[K\Delta - V_c \frac{\partial}{\partial z} \right] n + 2h\delta(z) \frac{\partial}{\partial E} \left[b(E)n - c(E) \frac{\partial n}{\partial E} \right] \\
& = q^{\text{prim}} + 2h\delta(z) \left[q^{\text{sec}} + q^{\text{ter}} - \sum_{t \in \text{ISM}} n_t v \sigma_{\text{inel}} n \right]. \quad (11)
\end{aligned}$$

In the first line, Δ is the Laplacian operator in cylindrical coordinates and $b(E)$ is the first-order energy redistribution term,

$$b(E) = \left\langle \frac{dE}{dt} \right\rangle - E_k \left(\frac{2m + E_k}{m + E_k} \right) \frac{V_c}{3h} + (1 + \beta^2) \frac{K_{pp}}{E}, \quad (12)$$

which includes ionization losses on neutral hydrogen and Coulomb losses in the ionized ISM (first term), adiabatic losses (second term) and reacceleration (last term). There is also $c(E) = \beta^2 K_{pp}$, the second-order term for reacceleration, which depends on the momentum diffusion term,

$$K_{pp} = \frac{4 V_a^2 \beta^2 E^2}{3 K(R)} \frac{1}{\delta(4 - \delta^2)(4 - \delta)}, \quad (13)$$

mediated by an effective Alfvén velocity V_a [69], and with δ the slope of the diffusion coefficient $K(R)$ (see below) in the low energy regime.

In addition to the primary and secondary source terms, q^{prim} and q^{sec} , defined respectively in Eqs. (7) and (8), the transport Eq. (11) also includes the tertiary source term

$$\begin{aligned}
q_i^{\text{ter}}(E_i, \vec{x}) = \sum_t \left[\int_{E_i}^{\infty} dE'_i \frac{d\sigma_{it \rightarrow i}^{\text{ina}}}{dE_i}(E'_i) v'_i n_i(E'_i) - \right. \\
\left. - \sigma_{it \rightarrow i}^{\text{ina}}(E_i) v_i n_i(E_i) \right] n_t(\vec{x}), \quad (14)
\end{aligned}$$

which accounts for the redistribution in energy of antinuclei (both primary and secondary). The first term describes the scattering of antinuclei species i , from high energies E'_i down to energy E_i , through non-annihilating interactions, characterized by the differential inelastic non-annihilating cross-section $d\sigma_{it \rightarrow i}^{\text{ina}}/dE_i$. The second term describes the scattering of antinuclei, from energy E_i to lower energies, and is determined by the total inelastic non-annihilating cross-section $\sigma_{it \rightarrow i}^{\text{ina}}$.

B. IS flux calculation: transport parameters (and configurations)

The transport Eq. (11) is solved semi-analytically with the USINE code² [68]. The differential density per kinetic

energy per nucleon, calculated at Earth position, $n_{\odot} = n(z=0, r=R_{\odot})$, is converted into an interstellar (IS) flux via (assuming isotropy), $\Phi_{\text{IS}} = v/(4\pi) \times n_{\odot}$.

The IS flux depends on the transport parameters $K(R)$, V_a , V_c and L : the combination of parameters (K/L , V_a , V_c) are determined from secondary-to-primary ratios [70] (e.g., B/C), and the degeneracy between the normalisation of K and L is lifted from the use of CR clocks [71] (e.g., $^{10}\text{Be}/^9\text{Be}$). Following Ref. [72], the diffusion coefficient is taken to be a generic power law with a possible low-energy break (or alternatively a modification in the non-relativistic regime) and another one at high-rigidity:

$$\begin{aligned}
K(R) = K_0 \times \underbrace{\beta^\eta \times \left\{ 1 + \left(\frac{R}{R_l} \right)^{\frac{\delta_l - \delta}{s_l}} \right\}^{s_l}}_{\text{non-relativistic} \times \text{low-rigidity break}} \\
\times \underbrace{\left\{ \frac{R}{(R_0 = 1 \text{ GV})} \right\}^\delta}_{\text{intermediate}} \times \underbrace{\left\{ 1 + \left(\frac{R}{R_h} \right)^{\frac{\delta - \delta_h}{s_h}} \right\}^{-s_h}}_{\text{high-rigidity break}}. \quad (15)
\end{aligned}$$

In Ref. [72], the degeneracies when fitting this large number of free parameters was mitigated by adjusting separately the high-rigidity break parameters (R_h , δ_h , s_h)—whose uncertainties were found not to impact the lower-energy parameters—, by fixing the unconstrained smoothness of the low-rigidity break parameter to $s_l = 0.04$ (fast transition), and by exploring three benchmark configurations with different numbers of free parameters. Ref. [72] found that the current CR data were fit equally well by these configurations. Two of them have 6 free parameters, namely SLIM (K_0 , L , δ , R_l , δ_l , s_l , enforcing $V_a = V_c = 0$) and QUIANT (K_0 , L , δ , η , and V_c , V_a , enforcing no low-rigidity break), whereas BIG has 8 parameters (K_0 , L , δ , R_l , δ_l , s_l , V_c , V_a , enforcing $\eta = 1$).

The value of all the above parameters (and uncertainties) are taken from a fit to (Li,Be,B)/C and $^{10}\text{Be}/^9\text{Be}$ data [73, 74]. The secondary antiproton flux was calculated following the steps described in Ref. [18]. The main advantage of this approach is that it keeps track of the full covariance of systematics uncertainties on the modelled background (i.e., including production cross-section, transport and primary flux uncertainties, along with their correlations). The latter is critical to have a statistically sound and relevant assessment of the presence or absence of a DM primary component in the data [18, 20]. As CR antinuclei have not been detected yet, we do not repeat the time-consuming steps to have their associated covariance matrices, but consider the total uncertainties only. To calculate them, a first good approximation is to add quadratically the specific production cross-section uncertainties of the antinuclei (see Sect. IV) to the transport and (propagated) primary flux uncertainties of the secondary antiprotons (as shown in Fig. 2 of Ref. [18]).

² <https://dmaurin.gitlab.io/USINE/>

For the calculation of the primary component, we follow closely the steps described in [20]. Namely, we use the source term discussed in Sect. III to calculate the fluxes on a grid of relevant DM parameters and L values (the latter being only loosely constrained, while critical in the calculation [75, 76]). We then rely on interpolations of these tabulated fluxes, so that we can explore different configurations and comparisons to the data in at most a minute (see next section).

There are several improvements in our analysis, compared to that of [20], beside the extension of the calculation to heavier antinuclei:

- First, we updated the DM source term (Sect. III), which however has a minor impact on the primary antiproton flux prediction.
- Second, compared to the USINE version used in Ref. [20] to constrain DM from antiprotons, we fixed a bug for the primary component calculation, slightly impacting the limits derived at low energy; we stress that this bug was already fixed in a recent analysis to set constraints on PBH-induced antiprotons and antideuterons [47]. We also include in USINE the propagation of ${}^3\text{He}$, whose inelastic cross-section on H and He is taken from Ref. [77].
- Third, the default transport configuration used for the secondary and primary calculations was taken to be BIG. While this configuration gave a perfect match (statistically-wise) between the secondary production and the AMS-02 antiproton first data release (four years of data, [6]), it was already shown in Ref. [20] to slightly overshoot (visually) and provide a less satisfactory fit to the latest complete AMS-02 dataset (seven years of data, [7]). We find here (see Fig. 1 and next section) that the secondary flux in the QUAIN T configuration gives a fairer visual match to these data³, and it also provides a slightly better fit to the data. Looking more closely at the χ^2_{\min} of these configurations, we recall that they were performing similarly on the secondary-to-primary (Table 1 of [73]) and radioactive (Table 3 of [74]) species. Nonetheless, the main visual difference between QUAIN T and the two other configurations is that the former displays a smoother transition than the latter, as reflected from the fact that $K(R)$ has no break (see Fig. 3 of [73]).

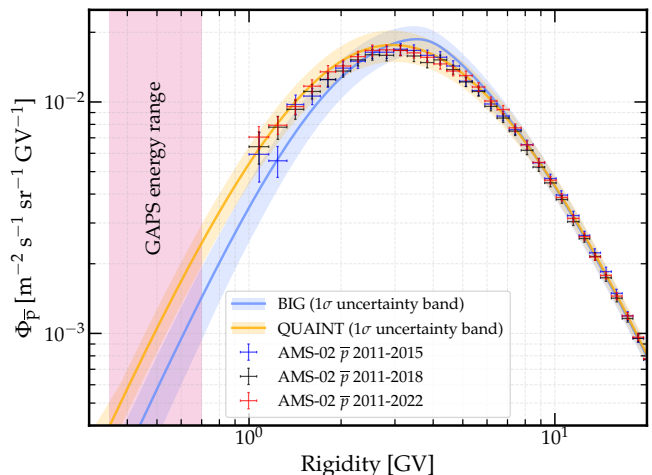


Figure 1. **TOA secondary antiproton fluxes** computed with BIG and QUAIN T propagation models, alongside their 1σ theoretical uncertainty bands. Solar modulation is modeled considering $\phi_{\text{FF}} = 678$ MV, appropriate for the 2011–2018 period (see text). Data points are from AMS-02, for three different data taking periods: 2011–2015 (blue symbols) [6], 2011–2018 (black symbols) [7], and 2011–2022 (red symbols) [78]. The magenta vertical band shows the GAPS energy range for \bar{p} detection.

C. TOA fluxes: Solar modulation

To obtain the TOA fluxes, we modulate the IS fluxes using the force-field approximation (FFA) [79, 80]. The Fisk parameter corresponding to the AMS-02 antiproton data-taking periods is calculated from neutron monitor data [81, 82] and retrieved from the Cosmic-Ray Data Base (CRDB) interface⁴ [83–85]. The first AMS-02 antiproton dataset was taken between 2011/05/19 and 2015/05/26 [6], while the second covers the period from 2011/05/19 to 2018/05/19 [7]. A third dataset has been published over the 11-year solar cycle 2011–2022 [78], but since it is kinematically limited up to ≈ 40 GV, we maintain the 2011–2018 release as our reference dataset. Focusing on the two broader datasets, the measurements from the KIEL, OULU, ROME, and SOPO stations yield an average Fisk potential of $\phi_{\text{FF}} \approx 722 \pm 25$ MV for the 2011–2015 period, and $\phi_{\text{FF}} \approx 678 \pm 25$ MV for the 2011–2018 period; hence a difference of 44 MV between the two datasets. This is smaller than the 100 MV uncertainty from the NM analysis [82]. We recall that the latter uncertainty was included as a nuisance parameter in the determination of the transport parameters [73]. As a result, this uncertainty is automatically accounted for in the covariance matrix of the model uncertainties.

A more critical issue is that of the validity of using, as we do, the same modulation potential for differently

³ For the danger of drawing hasty conclusions based on the visual inspection that do not account for the covariance matrix of uncertainties (and for alternative safer visual representations), we refer the reader to [18] and their Fig. 2.

⁴ <https://lpsc.in2p3.fr/crdb/>

charged particles. The Bartels-rotation averaged AMS-02 proton, antiproton, electron, and positron data over 11 years (corresponding to 139 Bartels rotations) [78] enable to test the limitation of the FFA [86] or the successfulness of its simplest extensions [87–89] and full modelling (e.g., Refs. [90, 91]). Ref. [86] highlighted that up to November 2015, the Fisk potential to fit proton and antiprotons differ by $\lesssim 80$ MV, but by more than 200 MV after. Over the 7 years of the most precise antiproton dataset, this amounts to a ~ 110 MV difference. This is within the above-mentioned uncertainty band, which, we recall, is smaller than the rest of the uncertainties. However, this is starting to reach an uncomfortable difference, and future AMS-02 release including data from periods of high-Solar activity will render this issue more acute, not to say critical.

It is interesting to stress that the analyses in Refs. [86, 92] both point at the importance of using at least the simplest extensions of the FFA, owing to its role in the significance of a potential DM signal in AMS-02 data. However, the analysis of Ref. [92] indicates that accounting for energy correlations in the data mitigates the impact of using different Solar modulation models (including the FFA). At this stage, the comprehensiveness of our analysis, which accounts for the propagation of cross-section, propagation and even Solar modulation uncertainties (though in the limited FFA), and also for the covariance matrix of systematic uncertainties on the data (in a more data-driven way than in [92]), does not call for an improved treatment of (the still debated) Solar modulation effects.

Fig. 1 displays the solar-modulated fluxes of secondary antiprotons predicted with the BIG and QUAINT propagation models. The 1σ theoretical uncertainties, discussed in Sect. VB, are shown as colored bands. For comparison, we overlay all the available AMS-02 datasets from different data-taking periods [6, 7, 78]. The solar modulation is modeled considering $\phi_{\text{FF}} = 678$ MV, to maintain consistency with the 2011–2018 AMS-02 dataset [7]. Finally, the shaded vertical band highlights the \bar{p} rigidity window targeted by the GAPS experiment.

VI. RESULTS ON ANTIPROTON FLUXES

Relying on the propagation framework, production cross-sections, and primary source spectra established in the previous sections, we now have all the ingredients to evaluate the primary and secondary TOA fluxes for antiprotons and, more generally, heavier antinuclei. Focusing first on the antiproton channel, we start by deriving updated upper limits on the DM annihilation cross-section, $\langle\sigma v\rangle$, as detailed below.

A. Derivation of upper limits on $\langle\sigma v\rangle$ from antiproton data: methodology

To compute updated 95% confidence level (CL) upper limits on $\langle\sigma v\rangle$, we follow the statistical procedure outlined in Ref. [20] (see also Ref. [47] for a similar application), considering the AMS-02 2011–2018 antiproton dataset [7]. We briefly recall the main steps below.

The primary antiproton fluxes depend on m_χ , $\langle\sigma v\rangle$, and the propagation parameters, most notably the diffusion halo half-height L [93]. Because the primary signal scales linearly with $\langle\sigma v\rangle$, we optimize the analysis by pre-computing a dense grid of flux predictions spanning the relevant parameter space of m_χ (5 GeV–10 TeV) and L (1–12 kpc). We then define a log-likelihood function that combines the χ^2 statistic with a penalty term for L :

$$-2 \ln \mathcal{L}(L, \mu) = \sum_{i,j} x_i (\mathcal{C}^{-1})_{ij} x_j + \left(\frac{\log L - \log \hat{L}}{\sigma_{\log L}} \right)^2,$$

where $x_i = \Phi_i^{\text{exp}} - \Phi_i^{\text{th}}(L, \mu)$, with Φ_i denoting the flux value in the i -th energy bin. The parameter array μ collectively represents the DM properties under investigation, namely $\langle\sigma v\rangle$ and m_χ . The covariance matrix \mathcal{C} accounts for both data uncertainties (statistical and systematic) and theoretical uncertainties on the modeled background (see Sect. VB). The central value \hat{L} and its standard deviation $\sigma_{\log L}$ are taken from Ref. [74], and depend on the chosen transport model.

To compute the upper limit on $\langle\sigma v\rangle$ for a fixed DM mass m_χ , we utilize the profile likelihood ratio (LR) test statistic:

$$\text{LR}(\langle\sigma v\rangle) = -2 \ln \mathcal{L}(L_{\min}, \langle\sigma v\rangle) + 2 \ln \mathcal{L}(L', \langle\sigma v\rangle'),$$

where the first term is evaluated at the halo size L_{\min} that maximizes the likelihood for the given $\langle\sigma v\rangle$, and the second term is evaluated considering the global best-fit parameters $(L', \langle\sigma v\rangle')$. Assuming Wilks' theorem, the LR follows a χ^2 distribution with one degree of freedom. In this way, we determine the 95% CL upper limits by requiring $\text{LR} = 3.84$.

B. Results on $\langle\sigma v\rangle$ upper limits

The resulting constraints are plotted in Fig. 2, which displays the upper limits on $\langle\sigma v\rangle$ as a function of m_χ ranging from 5 GeV to 10 TeV, assuming annihilation into the $b\bar{b}$ channel. The solid lines represent the bounds derived for the BIG and QUAINT propagation models. The dashed lines illustrate the projected impact of incorporating simulated GAPS \bar{p} data, as detailed in Sect. VID. Additionally, Fig. 3 presents the corresponding constraints for alternative annihilation channels.

Focusing on the solid lines in Fig. 2, the impact of the chosen propagation model on the constraints becomes evident. The BIG model yields less stringent bounds on

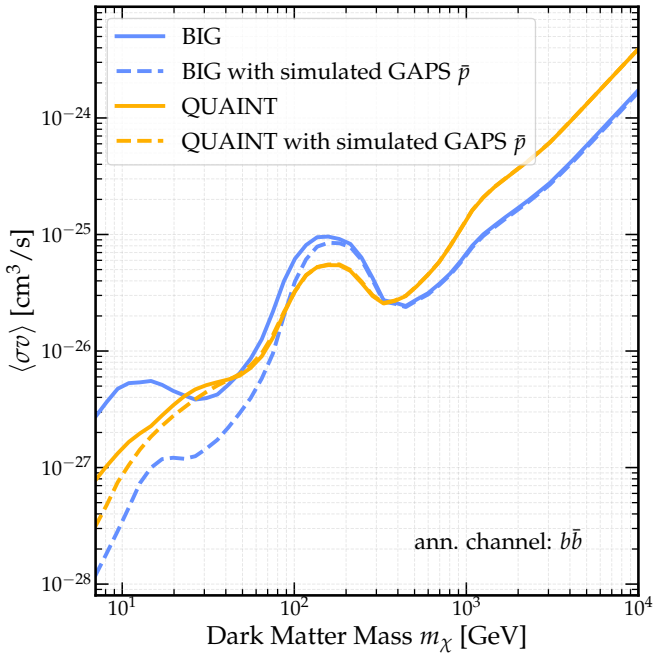


Figure 2. 95% CL upper limits on $\langle\sigma v\rangle$ as a function of m_χ , assuming the $b\bar{b}$ final state. Solid lines represent the constraints obtained from the analysis of AMS-02 \bar{p} data [7] alone. Dashed lines indicate the projected sensitivity gain achieved by including simulated \bar{p} data from GAPS. Results are shown for both the BIG (blue) and QUAINT (yellow) propagation models.

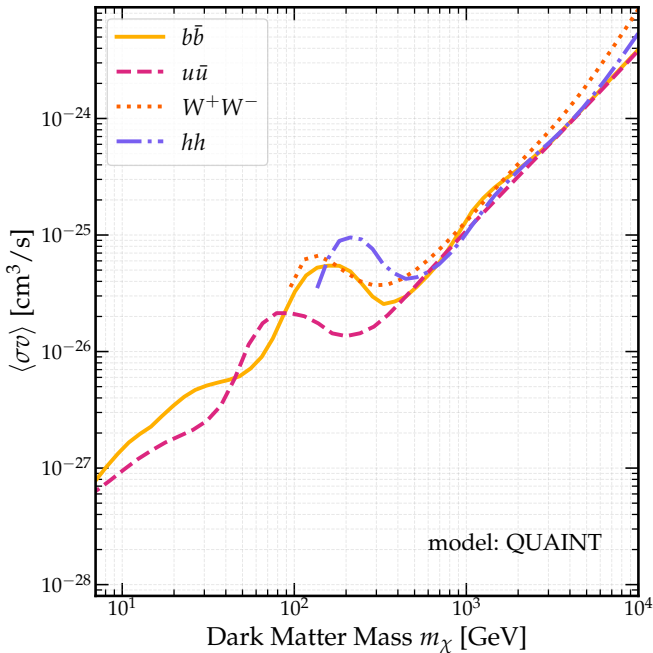


Figure 3. 95% CL upper limits on $\langle\sigma v\rangle$ as a function of m_χ , obtained with the QUAINT propagation model, assuming the $b\bar{b}$ (solid yellow line), $u\bar{u}$ (dashed magenta), W^+W^- (orange dotted) and hh (purple dot-dashed) final states.

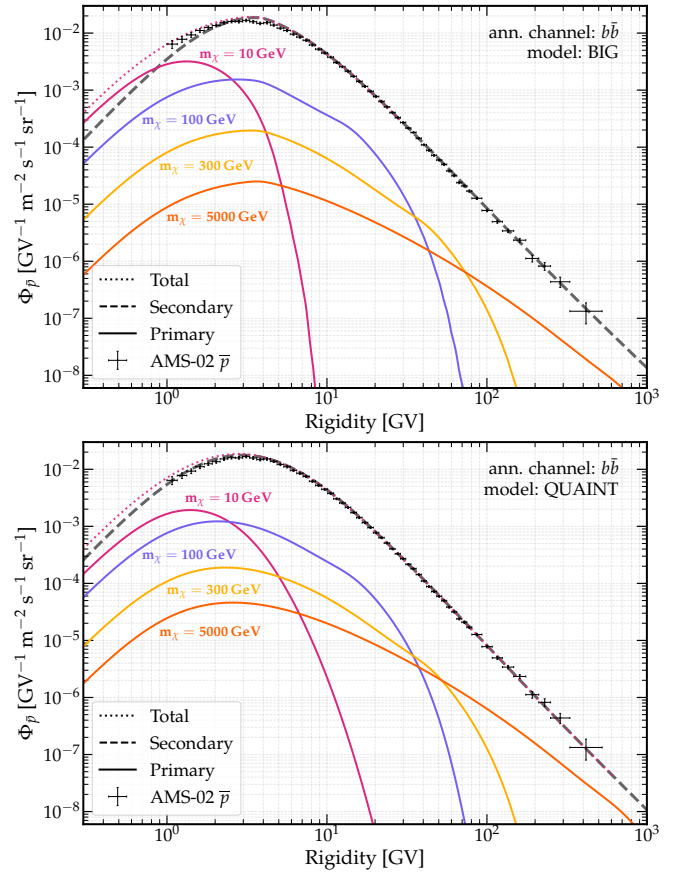


Figure 4. TOA antiproton fluxes evaluated for the BIG (upper panel) and QUAINT (lower panel) propagation models. Theoretical predictions include the secondary flux (gray dashed lines) and the primary contribution from DM annihilation into the $b\bar{b}$ channel (solid lines). The primary fluxes are obtained for the 95% CL upper limits on $\langle\sigma v\rangle$. The DM masses considered are $m_\chi = 10$ (magenta), 100 (purple), 300 (yellow), and 5000 GeV (orange). For the 10 GeV case, the total flux (primary + secondary) is indicated by the dotted magenta line. AMS-02 data [7] are shown for comparison. Solar modulation is treated considering $\phi_{\text{FF}} = 0.678$ GV.

$\langle\sigma v\rangle$ for lower DM masses, especially for $m_\chi \lesssim 20$ GeV, whereas the QUAINT model permits a larger DM contribution in the high-mass regime ($m_\chi \gtrsim 300$ GeV).

To understand these spectral features, it is useful to examine the underlying fluxes. Figure 4 displays the predicted secondary, primary, and total TOA fluxes of antiprotons for selected DM masses, for both BIG and QUAINT models. For each DM mass, the primary fluxes are computed at the corresponding 95% CL upper limits on $\langle\sigma v\rangle$ and the associated profile-likelihood value of the diffusion halo half-height L_{min} .

Examining the physical behavior, the BIG model exhibits a low-rigidity diffusion break around 4 GV, which produces a noticeable kink in the flux. This feature is also present in the secondary component, which is steeper at $R \lesssim 4$ GV than that of the QUAINT model. Consequently, the secondary flux in the BIG model leaves more

room for a DM contribution in this rigidity range. This leads to less stringent bounds on $\langle\sigma v\rangle$ for $m_\chi \lesssim 20$ GeV, as observed in Fig. 2. Conversely, the QUAINT model provides tighter constraints because the corresponding secondary flux follows the AMS-02 measurements more closely in the lower rigidity bins. Finally, for masses $m_\chi \gtrsim 300$ GeV, the QUAINT framework becomes less constraining, thus allowing for a slightly larger primary DM contribution. This effect is noticeable for $m_\chi = 5000$ GeV in Fig. 4.

It is important to emphasize that the secondary fluxes are derived prior to the present analysis: they are *predicted* and intentionally *not fitted* to the antiproton data. As discussed in Sect. VB, neither model is statistically strongly preferred by current nuclei or antiproton data. Therefore, we utilize both to bracket the systematic uncertainty associated with the transport setup.

C. Discussion on spectral features effects on $\langle\sigma v\rangle$ upper limits

To discuss more in detail the spectral features effects on the determination of the $\langle\sigma v\rangle$ constraints, Fig. 5 shows a visual breakdown of how the exclusion limits are formed. Although the bottom panel simplifies the analysis by neglecting the full covariance matrix of the data, the comparison of these three panels effectively highlights the correlation between the spectral features of the primary and secondary \bar{p} fluxes and the resulting shape of the constraints. In particular, it helps clarifying the origin of the weakening of the limits at approximately 80–250 GeV in m_χ , a feature also present in other works where correlations in AMS-02 data were not considered, such as Ref. [94]. The first two panels visually show the correspondence between the shape of the constraint curve (top panel) and the position of the peaks of the primary fluxes rescaled by R^3 (middle panel), computed using the upper limit values of $\langle\sigma v\rangle$ and the associated value of L_{\min} . From the plot of the residuals (third panel), it is possible to visually infer the origin of the spectral shape of the constraints, which results from the interplay between the position of the primary flux peaks and the shape of the predicted secondary background. Specifically, the weakening of the constraints at $m_\chi \approx 80$ –250 GeV in the top panel corresponds to a region in the third panel at $R \approx 10$ –40 GV, aligning more closely (within the 1σ experimental uncertainty) to the AMS-02 mean value, thus leaving room for a larger DM contribution in the upper limit analysis.

In conclusion, although the exact correspondence between residuals and limits is inevitably smoothed by data correlations and secondary uncertainties, this visualization successfully captures the most significant qualitative effects, providing an effective insight into the physical origin of the constraints' shape.

D. Result with simulated \bar{p} GAPS data

Having established the constraints from current AMS-02 data, we explore the discovery reach of the upcoming GAPS experiment. GAPS specifically targets the sub-GV antiproton window, where the secondary background is significantly suppressed, thereby maximizing the sensitivity to light DM signals. To quantitatively gauge the impact of these future measurements on the $\langle\sigma v\rangle$ constraints, we construct an illustrative scenario projecting the instrument's sensitivity onto the BIG and QUAINT background models, explained as follows.

We extract the projected energy positions, flux values, and relative errors of simulated GAPS data from Fig. 9 in Ref. [95]. Following the Asimov dataset approach [96], we generate a single representative mock dataset for each transport setup by forcing the GAPS data points to exactly match the median expected values of our secondary backgrounds. We treat the projected GAPS relative uncertainties as uncorrelated statistical errors. By neglecting correlated systematic uncertainties, this procedure yields an optimistic projection of the exclusion limits. Furthermore, because of the ambiguity regarding the exact solar modulation conditions during the upcoming GAPS flights, we adopt the AMS-02 modulation levels as a standardized baseline.

The results of this exercise are shown as dashed lines in Fig. 2. For the BIG model, the addition of these simulated low-energy data can significantly improve the constraints on $\langle\sigma v\rangle$ for low DM masses, even more than one order of magnitude. This is due to the steeper secondary flux shape in the sub-GV region, which results in stronger constraints. At the same time, the improvement in the DM bound by using the extrapolated background can also be rephrased by saying that for DM masses $\lesssim 50$ GeV, GAPS potentially has an excellent chance of detecting a DM signal in the antiproton channel. Conversely, for the QUAINT model, the effect is milder since the predicted background flux is higher.

To visualize this impact, Fig. 6 displays the mock GAPS data projected onto the BIG secondary background, alongside the 2011–2018 AMS-02 measurements [7]. The plot clearly illustrates how the addition of sub-GV data restricts the maximum allowed primary DM fluxes. This constraining power is particularly pronounced for lighter DM candidates, such as the $m_\chi = 10$ GeV case, because their annihilation spectra peak closer to the energy window of GAPS.

VII. RESULTS ON ANTIDEUTERON FLUXES

Having established robust upper limits on $\langle\sigma v\rangle$ from the antiproton channel, we now turn to antideuterons. We aim to determine whether a primary \bar{D} signal could still fall within the reach of current or near-future detectors without violating the stringent \bar{p} bounds derived above.

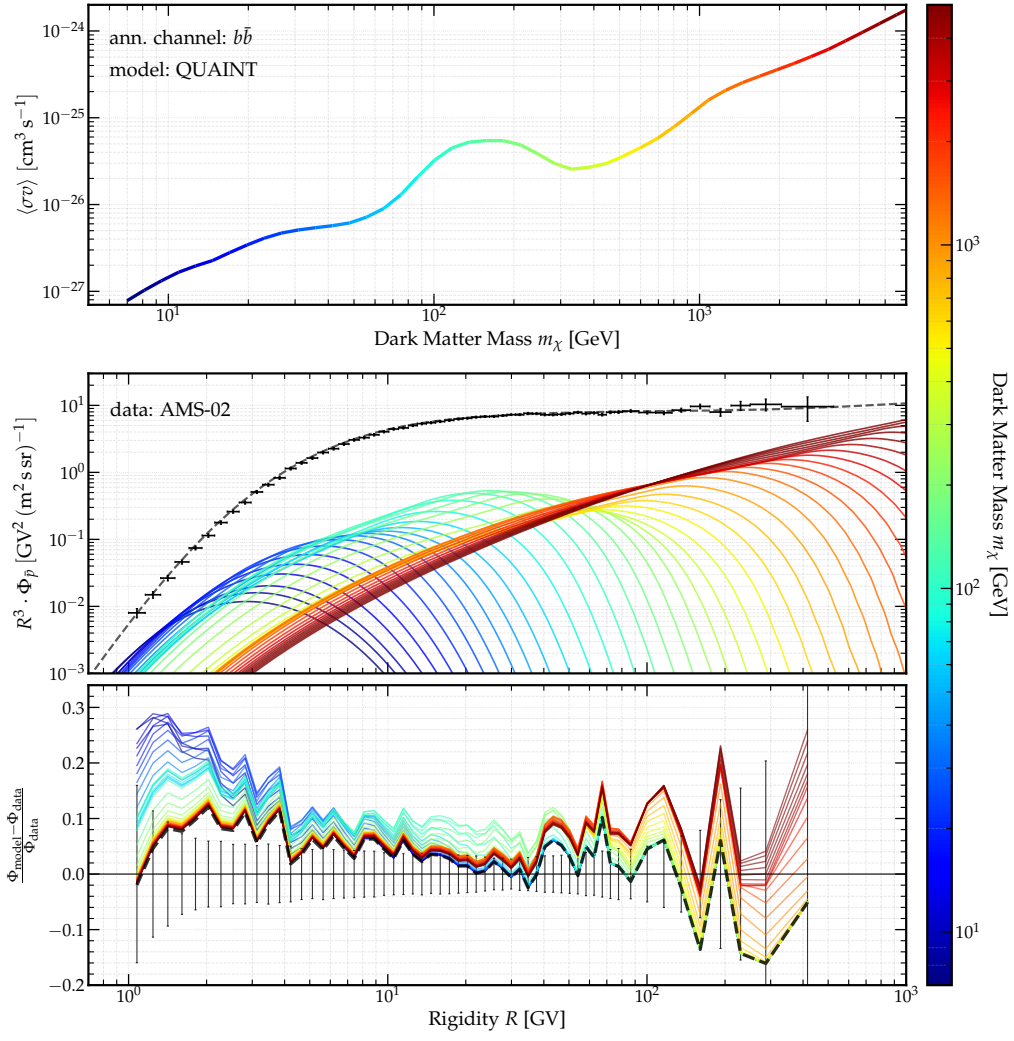


Figure 5. **Top panel:** upper limits on $\langle\sigma v\rangle$ obtained in our antiproton analysis for the QUAINT transport model, as a function of the DM mass m_χ . **Middle panel:** primary antiproton fluxes for various DM masses ranging from 7 to 5000 GeV (see the color bar on the right for the mass-color correspondence). These fluxes have been computed assuming the upper limit value of $\langle\sigma v\rangle$ corresponding to each mass, as shown in the top panel. The fluxes are rescaled by a factor of R^3 . The gray dashed line represents the secondary background reference flux (predicted, not fitted to the data). Black markers indicate the AMS-02 data [7]. **Bottom panel:** residuals from the comparison between the total fluxes (secondary + primary at the upper limit level) and the AMS-02 data. The black dashed line represents the residuals of the secondary reference flux alone. These residuals have been directly calculated without including the effect of the data covariance matrix and, for visual clarity, without showing the uncertainties on the secondary fluxes.

To address this, we compute the maximum allowed primary \bar{D} fluxes. For each DM mass m_χ , we adopt the 95% CL upper limit on $\langle\sigma v\rangle$ alongside the corresponding profile-likelihood value of the halo half-height L_{\min} . Given the uncertainty regarding the exact solar activity during the projected GAPS flights, we adopt a reference Force-Field modulation potential of $\phi_{\text{FF}} = 750$ MV for the following evaluations. Figure 7 (8) illustrates these upper-bound primary antideuteron fluxes for selected DM masses for the $b\bar{b}$ ($u\bar{u}$) annihilation channel, displaying the maximum expected signal against the secondary background. The plots also include the projected experimental sensitivities: the expected reach of three

balloon flights for GAPS [97], and the projected 2030 flux sensitivity for AMS-02, which accounts for its planned acceptance upgrade [12, 13].

Focusing first on the secondary background, the flux peaks at approximately 4 GeV/ n , approaching the sensitivities of AMS-02 and GAPS for both propagation models. The plots display the theoretical uncertainty band, whose computation is detailed in Sect. VB. To bracket the systematic uncertainty arising from the coalescence process, we evaluated the envelope of the predictions obtained from different coalescence models (namely, the $\Delta p + \Delta r$, Gaussian-Wigner, and Argonne-Wigner models), adopting the Gaussian model as the

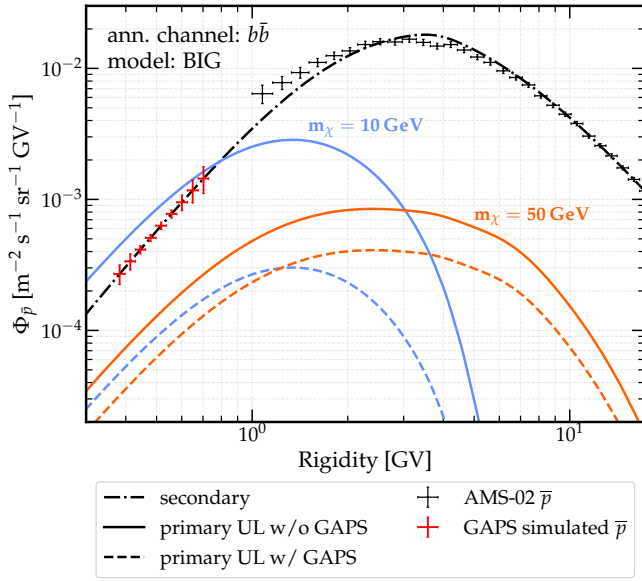


Figure 6. **Effect of mock GAPS data on the maximum allowed primary TOA antiproton fluxes**, evaluated for the BIG propagation model. Solid lines represent the maximum primary fluxes derived considering AMS-02 data alone, whereas dashed lines illustrate the constraints obtained considering the mock GAPS dataset in the $\langle\sigma v\rangle$ bound computation. The plot displays the mock GAPS data (red crosses) superimposed on the predicted secondary background (dash-dotted black line), alongside the AMS-02 data [7] (black crosses). The primary fluxes are computed for two representative masses of 10 and 50 GeV annihilating into $b\bar{b}$, and at the 95% CL upper limits on $\langle\sigma v\rangle$ as in Fig. 2.

central baseline.

Considering Fig. 7, for both propagation models the maximum allowed primary signal exhibits a strong mass dependence: the lower the DM mass, the larger the maximum predicted excess over the secondary background at sub-GeV energies. For instance, in the case of an 10 GeV DM candidate, the primary flux can exceed the background by up to three orders of magnitude. This clearly reaffirms the role of low-energy antideuterons as an almost background-free channel for indirect DM detection [21].

Comparing these maximum allowed primary fluxes with experimental sensitivities reveals a significant dependence on the underlying propagation framework. Under the BIG model, which yields less stringent $\langle\sigma v\rangle$ constraints for DM masses $m_\chi \lesssim 20$ GeV, the primary spectra can reach the projected GAPS sensitivity for very light DM candidates. Conversely, the QUANT model yields tighter low-mass constraints, suppressing the maximum allowed fluxes below the GAPS detection threshold across the entire probed mass range.

The plots also illustrate the impact of the updated Λ_b tuning, discussed in Sect. III, on the primary antideuteron fluxes. This modification primarily affects

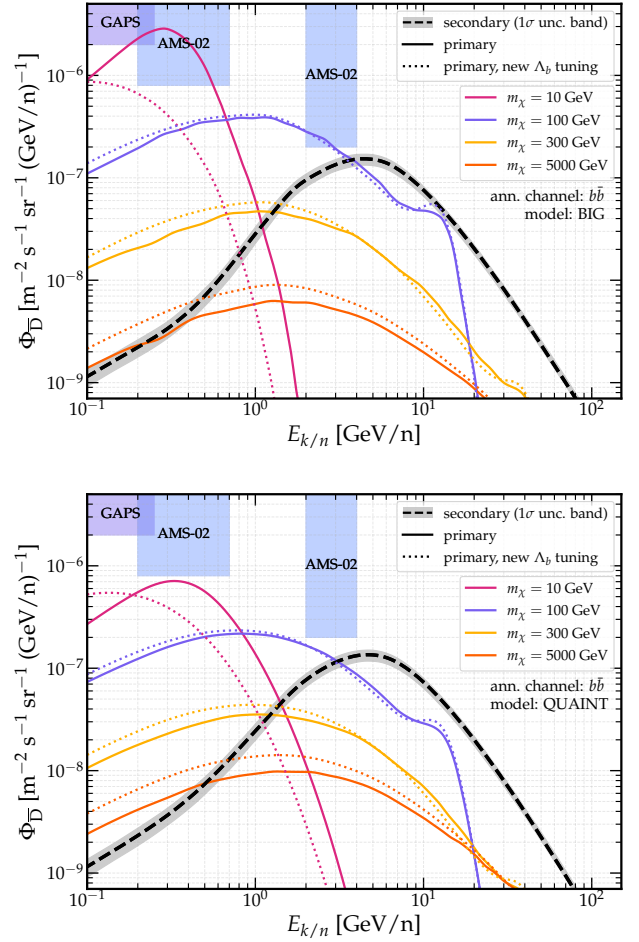


Figure 7. **TOA antideuteron fluxes.** The plot displays the expected secondary background flux (black dashed line) alongside primary fluxes from DM annihilation, considering the $b\bar{b}$ annihilation channel. The primary components are shown for both the standard `CosmIXs` spectra (solid lines) and the updated Λ_b tuning (dotted lines). All fluxes are evaluated at a solar modulation potential $\phi_{\text{FF}} = 750$ MV. The primary signals are computed using the 95% CL upper limits on $\langle\sigma v\rangle$ derived from our \bar{p} analysis. The gray band indicates the theoretical uncertainty on the secondary flux. The upper and lower panels present the results for the BIG and QUANT propagation models, respectively.

the spectra generated by light DM candidates, whereas the impact on heavier masses is substantially milder. This effect has important implications for indirect detection prospects, as the updated tuning suppresses the expected signal at masses $\lesssim 10$ GeV, rendering it inaccessible to both GAPS and AMS-02.

In Fig. 8 we show the productions for the \bar{D} generated from the $u\bar{u}$ channel. The main differences from the $b\bar{b}$ channel are the lower predicted fluxes for the lightest DM masses, which consequently fall below the projected GAPS sensitivity. This is due to the absence of \bar{D} con-

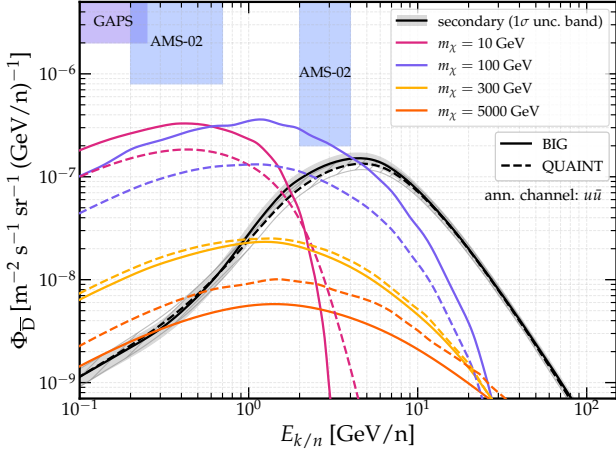


Figure 8. **TOA antideuteron fluxes.** The plot displays the expected secondary background fluxes (black lines) alongside primary fluxes from DM annihilation, considering the $u\bar{u}$ annihilation channel. The fluxes are shown for both the BIG (solid lines) and the QUAINT (dotted lines) propagation models. All fluxes are evaluated at a solar modulation potential $\phi_{\text{FF}} = 750$ MV. The primary signals are computed using the 95% CL upper limits on $\langle\sigma v\rangle$ derived from our \bar{p} analysis and employing the standard `CosmicS` spectra. The 1σ theoretical uncertainties on the secondary fluxes are represented by the gray bands: solid-filled for the BIG model and hatched for the QUAINT model.

tribution from Λ_b decays for the $u\bar{u}$ channel compared to the $b\bar{b}$ case, as also noticeable in the corresponding \bar{D} production spectra in Ref. [31].

The \bar{D} detection prospects are explicitly quantified in Fig. 9, which displays the maximum number of primary antideuterons that GAPS and AMS-02 are predicted to detect, assuming the current \bar{p} -derived constraints and considering the $b\bar{b}$ annihilation channel. The calculation of these expected event yields follows the methodology outlined in Ref. [98]. Specifically, the expected number of events is derived by integrating the theoretical primary flux over the kinetic energy window where the experiment is sensitive. This integrated flux is then divided by the corresponding experimental flux sensitivity. Finally, the result is multiplied by the baseline number of signal events defining that specific sensitivity threshold. As detailed therein, the flux sensitivities for antideuterons for both AMS-02 and GAPS are calibrated to correspond to 2 expected detection events.

Analyzing the projected yields, under the BIG propagation framework, GAPS is projected to detect at least one primary antideuteron only for light DM candidates with $m_\chi \lesssim 10$ GeV. In contrast, the QUAINT model yields a maximum signal that remains completely inaccessible to GAPS across the entire mass range. For AMS-02, however, both propagation models allow for the potential de-

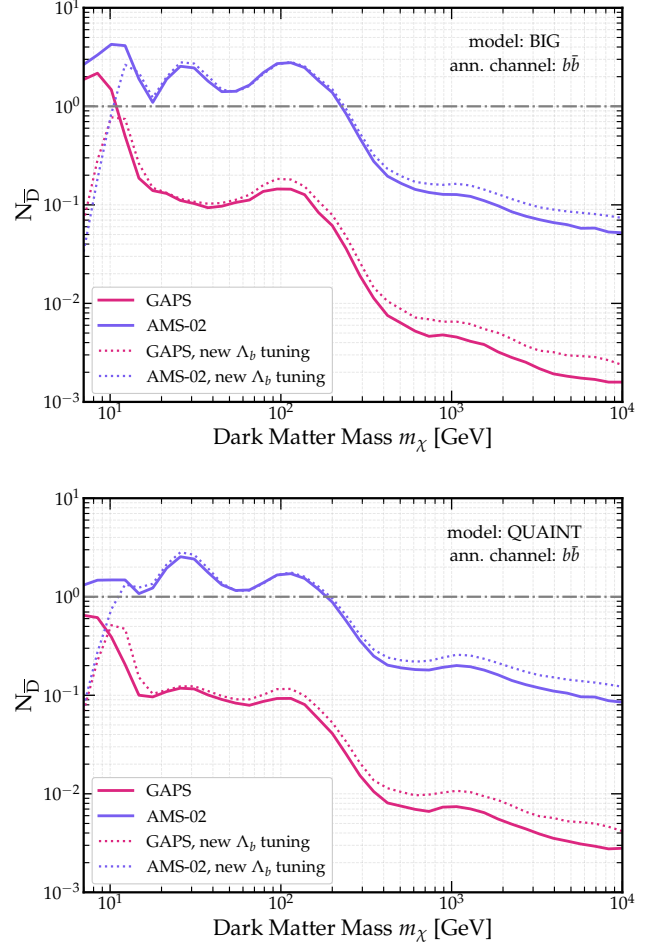


Figure 9. **Maximum expected number of detectable primary antideuterons ($N_{\bar{D}}$)** for the GAPS (magenta lines) and AMS-02 (purple lines) experiments as a function of the DM mass m_χ , computed considering $\phi_{\text{FF}} = 750$ MV. The solid lines indicate the yields computed using the standard `CosmicS` Λ_b tuning, while the dotted lines represent the results obtained with the updated Λ_b tuning. The upper and lower panels display the projections for the BIG and QUAINT propagation models, respectively.

tection of a primary antideuteron signal for DM masses up to $m_\chi \approx 200$ GeV.

Incorporating the updated Λ_b tuning reveals a strong suppression of the detection yields for DM masses $m_\chi \lesssim 15$ GeV. Specifically, for masses $m_\chi \lesssim 10$ GeV, this attenuation pushes the primary signal entirely below the 1-particle detection thresholds of both AMS-02 and GAPS. Consequently, since GAPS was exclusively sensitive to this specific low-mass window, this tuning renders the primary signal completely inaccessible to the GAPS experiment across the entire probed mass range.

Applying the same event yield methodology to the secondary astrophysical background, the expected number of events at AMS-02 is evaluated to be 1.12 ± 0.15 events under the QUAINT model and 1.31 ± 0.18 events

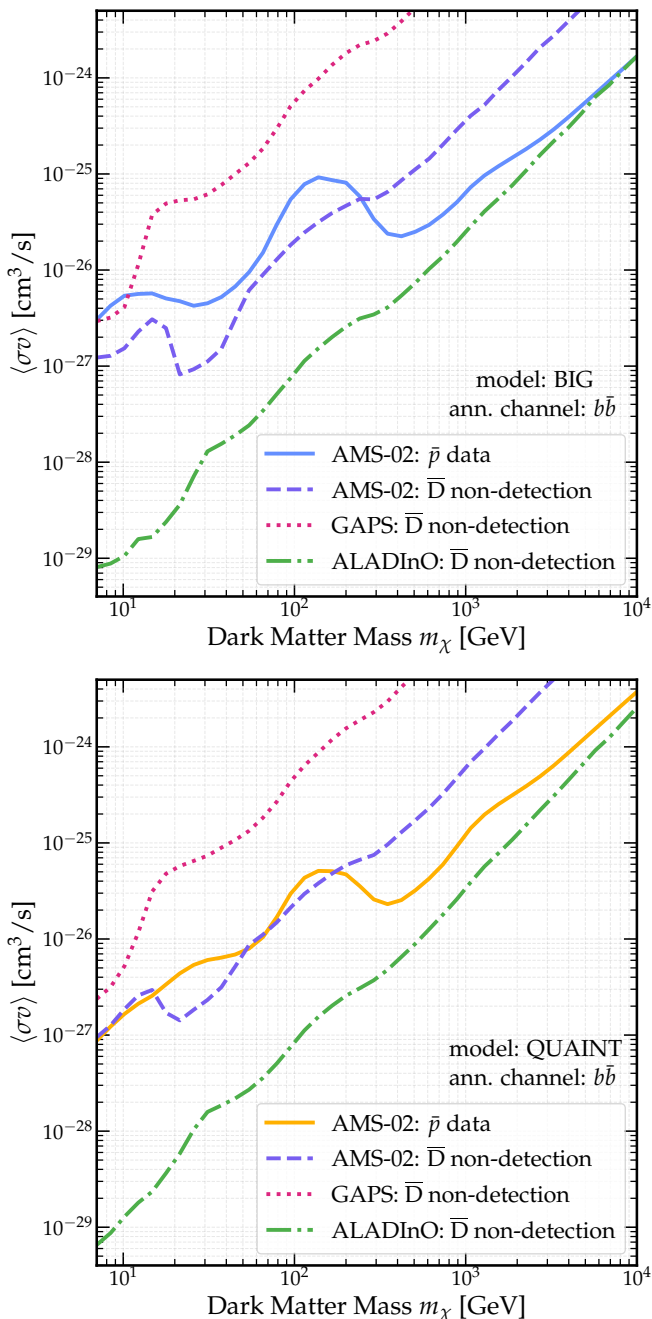


Figure 10. **95% CL upper limits on $\langle\sigma v\rangle$ as a function of m_χ** , assuming the $b\bar{b}$ final state. The solid lines represent the current constraints derived from the AMS-02 antiproton data. The other curves illustrate the projected upper limits assuming a null detection of primary antideuterons by current and future experiments: AMS-02 (dashed purple), GAPS (dotted magenta), and ALADInO (dash-dotted green). Results are displayed for the BIG (upper panel) and QUANT (lower panel) propagation models.

under the BIG framework. In contrast, the expected background at GAPS is suppressed by nearly three orders of magnitude relative to the detection threshold, firmly placing the experiment in a virtually background-free

regime.

Since AMS-02 and GAPS are projected to be sensitive to primary antideuterons, the absence of a detection can be exploited inversely to constrain the DM parameter space, yielding prospective upper limits on $\langle\sigma v\rangle$. To address this, Figure 10 presents the upper limits derived under the assumption of a null detection of antideuterons by each of these instruments independently. To compute these projected bounds, we adopted a single-bin approach: for each mass, the annihilation cross-section is rescaled such that the predicted total antideuteron flux reaches, but does not exceed, the sensitivity threshold of the respective experiment in its most constraining energy bin.

The results indicate that a confirmed non-detection by AMS-02 would improve the current \bar{p} -derived constraints for $m_\chi \lesssim 200$ GeV by up to a factor of ≈ 5 under the BIG model and ≈ 3 under QUANT, exhibiting a non-monotonic mass dependence. Conversely, a null result from GAPS would only tighten the existing limits in the very low mass regime, and strictly under the assumptions of the BIG model. Incorporating the projected capabilities of the proposed ALADInO experiment [99], a null detection under this simplified framework would drastically reduce the available DM parameter space, effectively constraining the thermal relic cross-section up to $m_\chi \approx 1000$ GeV.

VIII. RESULTS ON ANTIHELIUM FLUXES

As a final step, we assess the detectability of a potential ${}^3\bar{\text{He}}$ signal by computing the corresponding fluxes under the upper limits on $\langle\sigma v\rangle$ derived from \bar{p} data, and comparing them with the projected sensitivities of AMS-02 [98], GAPS [100], and ALADInO [99].

Given the $\mathcal{O}(10^{-4})$ suppression of the ${}^3\bar{\text{He}}$ multiplicity relative to \bar{D} in DM annihilation [38], deriving $\langle\sigma v\rangle$ limits directly from ${}^3\bar{\text{He}}$ null detection analyses is computationally prohibitive. We thus restrict our evaluation to a representative set of DM masses.

As shown in Fig. 11, the predicted TOA flux of primary ${}^3\bar{\text{He}}$ (for DM DM $\rightarrow b\bar{b}$) lies approximately three (four) orders of magnitude below the sensitivity of AMS-02 (GAPS). However, depending on the assumed propagation model, the flux could approach the sensitivity of the proposed ALADInO experiment.

An open issue concerns the unpublished claims by the AMS-02 collaboration regarding the detection of a dozen ${}^3\bar{\text{He}}$ events [101–103], which cannot be explained within our primary ${}^3\bar{\text{He}}$ production framework. Proposed mechanisms invoking an enhancement of ${}^3\bar{\text{He}}$ production from the decay of weakly-decaying b -hadrons [104, 105] appear to be in tension with the recent upper limit on the inclusive branching ratio of Λ_b^0 into ${}^3\bar{\text{He}}$ reported by the LHCb collaboration [60], as discussed in Ref. [38]. Other approaches that enhance the antinuclei production have

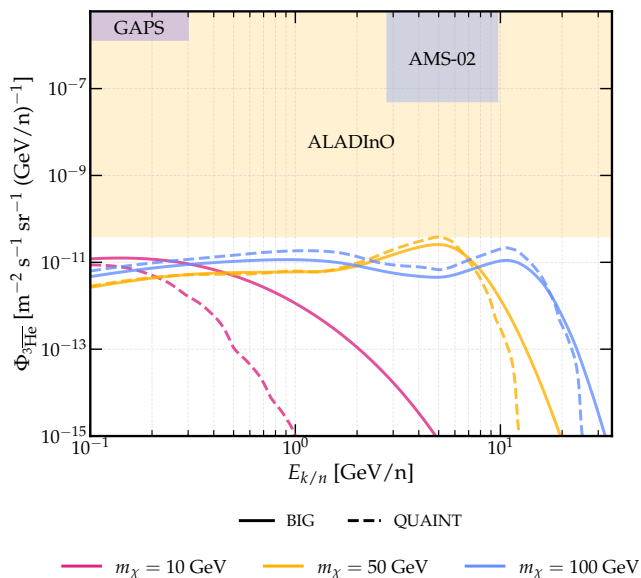


Figure 11. **Primary fluxes of TOA antihelium 3**, considering $m_\chi = 10, 50$, and 100 GeV and $\phi_{\text{FF}} = 750 \text{ MV}$, for the BIG and QUAINT models and using the Argonne coalescence approach. The fluxes are computed considering the 95 % CL upper limits on $\langle\sigma v\rangle$ obtained by our antiproton analysis.

been recently discussed in Ref. [98].

IX. CONCLUSIONS

In this work, we have revisited the production and detection prospects of cosmic-ray antinuclei—antiprotons, antideuterons, and antihelium—originating from both standard astrophysical processes and DM annihilation in the Galaxy. Building upon recent theoretical and experimental developments, we have provided updated predictions that incorporate improved modeling of particle production, coalescence mechanisms, and Galactic propagation.

On the production side, we employed state-of-the-art Monte Carlo simulations, to derive primary antinuclei yields from DM annihilation. We complemented this with updated differential cross-sections for secondary antideuteron production and a systematic comparison of coalescence approaches. In particular, the Argonne Wigner formalism provides a physically motivated benchmark for primary fluxes, while the residual model dependence is found to be at the level of $\mathcal{O}(20\%)$, consistent with recent studies. We have also implemented dedicated PYTHIA tunings, including the recent Λ_b -informed calibration.

For Galactic transport, we adopted the semi-analytical USINE framework and explored multiple propagation scenarios (BIG and QUAINT). These configurations provide comparably good fits to nuclei data but lead to non-negligible differences in the predicted secondary antiproton flux, which in turn impact the inferred DM con-

straints.

Using the AMS-02 antiproton data (2011–2018), we derived updated 95% CL upper limits on the DM annihilation cross-section $\langle\sigma v\rangle$ over the mass range $m_\chi \sim 5 \text{ GeV}–10 \text{ TeV}$. The resulting bounds reach $\langle\sigma v\rangle \sim \text{few} \times 10^{-26} \text{ cm}^3 \text{ s}^{-1}$ at $m_\chi \sim 100 \text{ GeV}$, with a clear dependence on the propagation setup: the BIG model yields weaker constraints below $m_\chi \lesssim 20 \text{ GeV}$, while QUAINT allows for larger DM contributions at $m_\chi \gtrsim 300 \text{ GeV}$. We also showed that the inclusion of simulated low-energy antiproton data from GAPS, could improve the limits by more than one order of magnitude for light DM candidates ($m_\chi \lesssim 50 \text{ GeV}$). Alternatively, this same result implies that, for this DM mass range, GAPS can potentially detect a DM signal in the antiproton channel.

We then translated these constraints into predictions for antideuterons. At sub-GeV/ n energies, the maximum allowed primary flux can exceed the secondary background by up to $\sim 2–3$ orders of magnitude for light DM candidates ($m_\chi \sim 10 \text{ GeV}$), confirming the well-known advantage of this channel. However, detectability strongly depends on the propagation model: within the BIG scenario, GAPS could detect $\mathcal{O}(1)$ primary antideuterons for $m_\chi \lesssim 10 \text{ GeV}$, whereas in the QUAINT setup the signal remains below the experimental sensitivity over the full mass range. AMS-02 retains sensitivity up to $m_\chi \sim 200 \text{ GeV}$. The updated Λ_b tuning significantly suppresses the predicted flux for $m_\chi \lesssim 10–15 \text{ GeV}$, pushing the expected signal below the detection threshold of both GAPS and AMS-02 in this region, for the $b\bar{b}$ annihilation channel.

We also quantified the projected impact of null detections. A non-observation of antideuterons by AMS-02 could strengthen current antiproton-derived bounds by up to a factor of $\sim 3–5$ for $m_\chi \lesssim 200 \text{ GeV}$, while GAPS would only improve constraints in the very low-mass regime and under favorable propagation assumptions. Future experiments such as ALADInO could probe cross-sections close to the thermal relic benchmark up to $m_\chi \sim 1 \text{ TeV}$.

For antihelium, we found that the predicted fluxes from DM annihilation are $\sim 3–4$ orders of magnitude below the sensitivities of AMS-02 and GAPS, although they may approach the reach of next-generation instruments. These results highlight a persistent tension with the tentative AMS-02 antihelium candidate events, which cannot be accommodated within standard coalescence-based production models for WIMPs. Nevertheless, enhanced antihelium production can be obtained in models endowed with confining dark sectors, like the SUEP model recently discussed in Ref. [98].

In conclusion, our analysis provides a unified and updated framework for interpreting cosmic-ray antinuclei measurements and emphasizes the complementarity between antiprotons and heavier antinuclei. Actually, several experiments are ongoing (or planned) to both improve the antiproton data and detect $A > 1$ antinuclei in cosmic rays. However, the foreseen difficulty to decrease

the modelling uncertainties on the secondary antiproton flux [106] makes heavier antinuclei the only guaranteed route to improve significantly (by up to two orders of magnitude) the DM constraints at low masses.

ACKNOWLEDGMENTS

M.D.M., F.D., N.F., J.K. and L.S. acknowledge support from the research grant *TAsP (Theoretical Astroparticle Physics)* funded by Istituto Nazionale di Fisica Nucleare (INFN). M.D.M. and J.K. acknowledge support from the Italian Ministry of University and Re-

search (MUR), PRIN 2022 “EXSKALIBUR – Euclid-Cross-SKA: Likelihood Inference Building for Universe’s Research”, Grant No. 20222BBYB9, CUP I53D23000610 0006, and from the European Union—Next Generation EU. J.K. acknowledges support from the Italian Space Agency through the ASI INFN agreement n. 2018-28-HH.0: “Partecipazione italiana al GAPS - General AntiParticle Spectrometer”. N.F. is supported by the Italian Ministry of University and Research (MUR) via the PRIN 2022 Project No. 20228WHTYC – CUP: D53C24003550006 and from the European Union—Next Generation EU.

-
- [1] O. Adriani *et al.*, *JETP Lett.* **96**, 621 (2013).
- [2] O. Adriani *et al.*, *Phys. Rev. Lett.* **102**, 051101 (2009), [arXiv:0810.4994 \[astro-ph\]](#).
- [3] O. Adriani *et al.* (PAMELA), *Nature* **458**, 607 (2009), [arXiv:0810.4995 \[astro-ph\]](#).
- [4] O. Adriani *et al.* (PAMELA), *Riv. Nuovo Cim.* **40**, 473 (2017), [arXiv:1801.10310 \[astro-ph.HE\]](#).
- [5] M. Aguilar, L. Ali Cavazonza, B. Alpat, G. Ambrosi, *et al.* (AMS Collaboration), *Phys. Rev. Lett.* **117**, 091103 (2016).
- [6] M. Aguilar *et al.* (AMS), *Phys. Rev. Lett.* **117**, 091103 (2016).
- [7] M. Aguilar *et al.* (AMS), *Phys. Rept.* **894**, 1 (2021).
- [8] K. Abe *et al.*, *Phys. Rev. Lett.* **108**, 131301 (2012), [arXiv:1201.2967 \[astro-ph.CO\]](#).
- [9] G. Osteria (GAPS), *Nucl. Instrum. Meth. A* **958**, 162201 (2020).
- [10] P. von Doetinchem *et al.*, *JCAP* **08**, 035 (2020), [arXiv:2002.04163 \[astro-ph.HE\]](#).
- [11] K. Sakai *et al.* (BESS Collaboration), *Phys. Rev. Lett.* **132**, 131001 (2024).
- [12] V. Choutko and F. Giovacchini, in *International Cosmic Ray Conference*, International Cosmic Ray Conference, Vol. 4 (2008) pp. 765–768.
- [13] A. Oliva, “Latest results of the Alpha Magnetic Spectrometer on the International Space Station,” (2024), invited talk at the JENAA Workshop @ CERN, 20 Aug 2024.
- [14] T. Aramaki, C. J. Hailey, S. E. Boggs, P. von Doetinchem, H. Fuke, S. I. Mognet, R. A. Ong, K. Perez, and J. Zweerink (GAPS), *Astropart. Phys.* **74**, 6 (2016), [arXiv:1506.02513 \[astro-ph.HE\]](#).
- [15] P. von Doetinchem *et al.*, *PoS ICRC2015*, 1218 (2016), [arXiv:1507.02712 \[hep-ph\]](#).
- [16] C. Hailey (GAPS), Invited talk at the Workshop <https://indico.cern.ch/event/1480110/overview>, CERN 22 Jan 2026 (2026).
- [17] F. Donato, D. Maurin, P. Brun, T. Delahaye, and P. Salati, *Phys. Rev. Lett.* **102**, 071301 (2009), [arXiv:0810.5292 \[astro-ph\]](#).
- [18] M. Boudaud, Y. Génolini, L. Derome, J. Lavalle, D. Maurin, P. Salati, and P. D. Serpico, *Phys. Rev. Res.* **2**, 023022 (2020), [arXiv:1906.07119 \[astro-ph.HE\]](#).
- [19] M. Di Mauro, M. Korsmeier, and A. Cuoco, *Phys. Rev. D* **109**, 123003 (2024), [arXiv:2311.17150 \[astro-ph.HE\]](#).
- [20] F. Calore, M. Cirelli, L. Derome, Y. Genolini, D. Maurin, P. Salati, and P. D. Serpico, *SciPost Phys.* **12**, 163 (2022), [arXiv:2202.03076 \[hep-ph\]](#).
- [21] F. Donato, N. Fornengo, and P. Salati, *Physical Review D* **62**, 043003 (2000), [arXiv:hep-ph/9904481 \[hep-ph\]](#).
- [22] M. Cirelli, N. Fornengo, M. Taoso, and A. Vittino, *Journal of High Energy Physics* **2014**, 009 (2014), [arXiv:1401.4017 \[hep-ph\]](#).
- [23] E. Carlson, A. Coogan, T. Linden, S. Profumo, A. Ibarra, and S. Wild, *Phys. Rev. D* **89**, 076005 (2014), [arXiv:1401.2461 \[hep-ph\]](#).
- [24] P. Chardonnet, J. Orloff, and P. Salati, *Phys. Lett. B* **409**, 313 (1997), [arXiv:astro-ph/9705110 \[astro-ph\]](#).
- [25] N. Fornengo, L. Maccione, and A. Vittino, *JCAP* **09**, 031 (2013), [arXiv:1306.4171 \[hep-ph\]](#).
- [26] M. Korsmeier, F. Donato, and N. Fornengo, *Phys. Rev. D* **97**, 103011 (2018), [arXiv:1711.08465 \[astro-ph.HE\]](#).
- [27] M. Kachelrieß, S. Ostapchenko, and J. Tjemsland, *JCAP* **08**, 048 (2020), [arXiv:2002.10481 \[hep-ph\]](#).
- [28] L. Šerkšnytė *et al.*, *Phys. Rev. D* **105**, 083021 (2022), [arXiv:2201.00925 \[astro-ph.HE\]](#).
- [29] P. De La Torre Luque, M. W. Winkler, and T. Linden, *JCAP* **10**, 017 (2024), [arXiv:2404.13114 \[astro-ph.HE\]](#).
- [30] D. Maurin, *Computer Physics Communications* **247**, 106942 (2020), [arXiv:1807.02968 \[astro-ph.IM\]](#).
- [31] M. Di Mauro, N. Fornengo, A. Jueid, R. R. de Austri, and F. Bellini, *Phys. Rev. Lett.* **135**, 131002 (2025), [arXiv:2411.04815 \[astro-ph.HE\]](#).
- [32] M. Di Mauro, J. Koechler, L. Stefanuto, F. Bellini, F. Donato, and N. Fornengo, *subm. to Phys. Rev. D* (2026), [arXiv:2603.19352 \[hep-ph\]](#).
- [33] S. Acharya *et al.* (ALICE), *Eur. Phys. J. C* **80**, 889 (2020), [arXiv:2003.03184 \[nucl-ex\]](#).
- [34] ALICE Collaboration, *Phys. Lett. B* **860**, 139191 (2025).
- [35] ALICE Collaboration, *Phys. Lett. B* **800**, 135043 (2019), [arXiv:1906.03136 \[nucl-ex\]](#).
- [36] A. Ibarra and S. Wild, *JCAP* **02**, 021 (2013), [arXiv:1209.5539 \[hep-ph\]](#).
- [37] R. Pohl *et al.* (CREMA), *Science* **353**, 669 (2016).
- [38] M. Di Mauro, A. Jueid, J. Koechler, and R. R. de Austri, *Phys. Rev. D* **112**, 083017 (2025), [arXiv:2504.07172 \[hep-ph\]](#).
- [39] R. Scheibl and U. W. Heinz, *Phys. Rev. C* **59**, 1585 (1999), [arXiv:nucl-th/9809092 \[nucl-th\]](#).

- [40] F. Bellini and A. P. Kalweit, *Phys. Rev. C* **99**, 054905 (2019), [arXiv:1807.05894 \[hep-ph\]](#).
- [41] K. Blum, K. C. Y. Ng, R. Sato, and M. Takimoto, *Phys. Rev. D* **96**, 103021 (2017), [arXiv:1704.05431 \[astro-ph.HE\]](#).
- [42] F. Bellini, K. Blum, A. P. Kalweit, and M. Puccio, *Phys. Rev. C* **103**, 014907 (2021), [arXiv:2007.01750 \[nucl-th\]](#).
- [43] M. Kachelrieß, S. Ostapchenko, and J. Tjemsland, *Eur. Phys. J. A* **56**, 4 (2020), [arXiv:1905.01192 \[hep-ph\]](#).
- [44] M. Mahlein, L. Barioglio, F. Bellini, L. Fabbietti, C. Pinto, B. Singh, and S. Tripathy, *Eur. Phys. J. C* **83**, 804 (2023), [arXiv:2302.12696 \[hep-ex\]](#).
- [45] R. B. Wiringa, V. G. J. Stoks, and R. Schiavilla, *Phys. Rev. C* **51**, 38 (1995), [arXiv:nucl-th/9408016](#).
- [46] M. Horst, L. Barioglio, F. Bellini, L. Fabbietti, C. Pinto, B. Singh, and S. Tripathy, *Eur. Phys. J. C* **83**, 804 (2023), [arXiv:2302.12696 \[hep-ex\]](#).
- [47] V. De Romeri, F. Donato, D. Maurin, L. Stefanuto, and A. Tolino, *Phys. Rev. D* **112**, 023003 (2025), [arXiv:2505.04692 \[hep-ph\]](#).
- [48] J. F. Navarro, C. S. Frenk, and S. D. M. White, *Astron. Astrophys. J.* **462**, 563 (1996), [arXiv:astro-ph/9508025](#).
- [49] P. J. McMillan, *Monthly Notices of the Royal Astronomical Society* **465**, 76–94 (2016).
- [50] P. F. de Salas and A. Widmark, *Reports on Progress in Physics* **84**, 104901 (2021), [arXiv:2012.11477 \[astro-ph.GA\]](#).
- [51] Gravity Collaboration, R. Abuter, *et al.*, *Astron. Astrophys.* **625**, L10 (2019), [arXiv:1904.05721 \[astro-ph.GA\]](#).
- [52] C. Bierlich *et al.*, *SciPost Phys. Codeb.* **2022**, 8 (2022), [arXiv:2203.11601 \[hep-ph\]](#).
- [53] C. Arina, M. Di Mauro, N. Fornengo, J. Heisig, A. Jueid, and R. R. de Austri, *JCAP* **03**, 035 (2024), [arXiv:2312.01153 \[astro-ph.HE\]](#).
- [54] C. Arina, M. Di Mauro, N. Fornengo, J. Heisig, A. Jueid, and R. R. de Austri (2025) [arXiv:2501.13281 \[hep-ph\]](#).
- [55] S. Schael *et al.* (ALEPH), *Phys. Lett. B* **639**, 192 (2006), [arXiv:hep-ex/0604023](#).
- [56] A. Jueid, J. Kip, R. R. de Austri, and P. Skands, *JCAP* **04**, 068 (2023), [arXiv:2202.11546 \[hep-ph\]](#).
- [57] A. Jueid, J. Kip, R. R. de Austri, and P. Skands, *JHEP* **02**, 119 (2024), [arXiv:2303.11363 \[hep-ph\]](#).
- [58] S. Amoroso, S. Caron, A. Jueid, R. Ruiz de Austri, and P. Skands, *JCAP* **05**, 007 (2019), [arXiv:1812.07424 \[hep-ph\]](#).
- [59] Y. S. Amhis *et al.* (HFLAV), *Eur. Phys. J. C* **81**, 226 (2021), [arXiv:1909.12524 \[hep-ex\]](#).
- [60] R.-D. Moise, *PoS ICHEP2024*, 676 (2025).
- [61] S. Acharya *et al.* (ALICE Collaboration), *Phys. Rev. C* **97**, 024615 (2018), [arXiv:1709.08522 \[nucl-ex\]](#).
- [62] L. Orusa, M. Di Mauro, F. Donato, and M. Korsmeier, *Phys. Rev. D* **105**, 123021 (2022), [arXiv:2203.13143 \[astro-ph.HE\]](#).
- [63] M. Korsmeier, F. Donato, and M. Di Mauro, *Phys. Rev. D* **97**, 103019 (2018), [arXiv:1802.03030 \[astro-ph.HE\]](#).
- [64] M. Di Mauro, J. Koechler, L. Stefanuto, F. Bellini, F. Donato, and N. Fornengo, “Differential cross-sections for secondary antiproton and antideuteron production,” (2026).
- [65] V. S. Berezinskii, S. V. Bulanov, V. A. Dogiel, and V. S. Ptuskin, *Amsterdam: North-Holland, 1990, edited by Ginzburg, V.L.* (Elsevier Science and Technology, 1990).
- [66] R. Schlickeiser, *Cosmic ray astrophysics / Reinhard Schlickeiser, Astronomy and Astrophysics Library; Physics and Astronomy Online Library. Berlin: Springer. ISBN 3-540-66465-3, 2002, XV + 519 pp.* (Springer, 2002).
- [67] A. W. Strong, I. V. Moskalenko, and V. S. Ptuskin, *Ann. Rev. Nucl. Part. Sci.* **57**, 285 (2007), [arXiv:astro-ph/0701517](#).
- [68] D. Maurin, *Comput. Phys. Commun.* **247**, 106942 (2020), [arXiv:1807.02968 \[astro-ph.IM\]](#).
- [69] E. S. Seo and V. S. Ptuskin, *Astrophys. J.* **431**, 705 (1994).
- [70] D. Maurin, F. Donato, R. Taillet, and P. Salati, *Astrophys. J.* **555**, 585 (2001), [arXiv:astro-ph/0101231](#).
- [71] F. Donato, D. Maurin, and R. Taillet, *Astron. Astrophys.* **381**, 539 (2002), [arXiv:astro-ph/0108079](#).
- [72] Y. Génolini, M. Boudaud, P. I. Batista, S. Caroff, L. Derome, J. Lavalle, A. Marcowith, D. Maurin, V. Poireau, V. Poulin, S. Rosier, P. Salati, P. D. Serpico, and M. Vecchi, *Phys. Rev. D* **99**, 123028 (2019), [arXiv:1904.08917 \[astro-ph.HE\]](#).
- [73] N. Weinrich, Y. Génolini, M. Boudaud, L. Derome, and D. Maurin, *Astron. Astrophys.* **639**, A131 (2020), [arXiv:2002.11406 \[astro-ph.HE\]](#).
- [74] N. Weinrich, M. Boudaud, L. Derome, Y. Génolini, J. Lavalle, D. Maurin, P. Salati, P. Serpico, and G. Weymann-Despres, *Astron. Astrophys.* **639**, A74 (2020), [arXiv:2004.00441 \[astro-ph.HE\]](#).
- [75] F. Donato, N. Fornengo, D. Maurin, and P. Salati, *Phys. Rev. D* **69**, 063501 (2004), [arXiv:astro-ph/0306207](#).
- [76] Y. Génolini, M. Boudaud, M. Cirelli, L. Derome, J. Lavalle, D. Maurin, P. Salati, and N. Weinrich, *Phys. Rev. D* **104**, 083005 (2021), [arXiv:2103.04108 \[astro-ph.HE\]](#).
- [77] S. Acharya *et al.* (ALICE), *Nature Phys.* **19**, 61 (2023), [arXiv:2202.01549 \[nucl-ex\]](#).
- [78] M. Aguilar *et al.* (AMS Collaboration), *Phys. Rev. Lett.* **134**, 051002 (2025).
- [79] L. J. Gleeson and W. I. Axford, *Astrophys. J.* **154**, 1011 (1968).
- [80] L. A. Fisk, *J. Geophys. Res.* **76**, 221 (1971).
- [81] D. Maurin, A. Cheminet, L. Derome, A. Ghelfi, and G. Hubert, *Adv. Space Res.* **55**, 363 (2015), [arXiv:1403.1612 \[astro-ph.EP\]](#).
- [82] A. Ghelfi, D. Maurin, A. Cheminet, L. Derome, G. Hubert, and F. Melot, *Advances in Space Research* **60**, 833 (2017), [arXiv:1607.01976 \[astro-ph.HE\]](#).
- [83] D. Maurin, F. Melot, and R. Taillet, *Astron. Astrophys.* **569**, A32 (2014), [arXiv:1302.5525 \[astro-ph.HE\]](#).
- [84] D. Maurin, H. P. Dembinski, J. Gonzalez, I. C. Mariş, and F. Melot, *Universe* **6**, 102 (2020), [arXiv:2005.14663 \[astro-ph.HE\]](#).
- [85] D. Maurin, M. Ahlers, H. Dembinski, A. Haungs, P.-S. Mangeard, F. Melot, P. Mertsch, D. Wochele, and J. Wochele, *European Physical Journal C* **83**, 971 (2023), [arXiv:2306.08901 \[astro-ph.HE\]](#).
- [86] I. John and A. Cuoco, *PoS ICRC2025*, 1304 (2025).
- [87] M. Kuhlen and P. Mertsch, *Phys. Rev. Lett.* **123**, 251104 (2019), [arXiv:1909.01154 \[astro-ph.HE\]](#).
- [88] I. Cholis, D. Hooper, and T. Linden, *JCAP* **10**, 051 (2022), [arXiv:2007.00669 \[astro-ph.HE\]](#).
- [89] W.-C. Long and J. Wu, *Phys. Rev. D* **109**, 083009 (2024), [arXiv:2403.20038 \[astro-ph.SR\]](#).

- [90] O. P. M. Aslam, M. S. Potgieter, X. Luo, and M. D. Ngobeni, *Astrophys. J.* **953**, 101 (2023), [arXiv:2303.13268 \[astro-ph.SR\]](#).
- [91] N. Tomassetti, B. Bertucci, E. Fiandrini, and B. Khiali, *Galaxies* **13**, 23 (2025), [arXiv:2503.14025 \[astro-ph.HE\]](#).
- [92] K.-K. Duan, X. Wang, W.-H. Li, Z.-H. Xu, Y.-L. S. Tsai, and Y.-Z. Fan, *JCAP* **10**, 049 (2025), [arXiv:2506.13352 \[astro-ph.CO\]](#).
- [93] Y. Génolini, M. Boudaud, M. Cirelli, L. Derome, J. Lavalle, D. Maurin, P. Salati, and N. Weinrich, *Physical Review D* **104** (2021), [10.1103/physrevd.104.083005](#).
- [94] S. Balan, F. Kahlhoefer, M. Korsmeier, S. Manconi, and K. Nippel, *JCAP* **08**, 052 (2023), [arXiv:2303.07362 \[hep-ph\]](#).
- [95] F. Rogers *et al.* (GAPS), *Astropart. Phys.* **145**, 102791 (2023), [arXiv:2206.12991 \[astro-ph.HE\]](#).
- [96] G. Cowan, K. Cranmer, E. Gross, and O. Vitells, *The European Physical Journal C* **71** (2011), [10.1140/epjc/s10052-011-1554-0](#).
- [97] T. Aramaki, C. Hailey, S. Boggs, P. von Doetinchem, H. Fuke, S. Mognet, R. Ong, K. Perez, *et al.*, *Appl. Phys.* **74**, 6 (2016).
- [98] M. D. Mauro, C. Gemell, A. Batz, D. Curtin, F. Donato, N. Fornengo, and G. D. Kribs, “Enhanced cosmic-ray antinuclei fluxes with dark matter annihilation into sneups,” (2026), [arXiv:2602.15132 \[hep-ph\]](#).
- [99] O. Adriani *et al.*, *Instruments* **6** (2022), [10.3390/instruments6020019](#).
- [100] N. Saffold *et al.* (GAPS), *Astroparticle Physics* **130**, 102580 (2021).
- [101] S. Ting, “The first five years of the alpha magnetic spectrometer on the international space station: Unlocking the secrets of the cosmos,” CERN (2016).
- [102] S. Lu, “Cosmic ray antideuteron search with alpha magnetic spectrometer (ams),” MIAPP (2022).
- [103] P. Zuccon, “Ams-02 results & upgrade,” MIAPP (2022).
- [104] M. W. Winkler and T. Linden, *Phys. Rev. Lett.* **126**, 101101 (2021), [arXiv:2006.16251 \[hep-ph\]](#).
- [105] M. W. Winkler and T. Linden, (2021), [arXiv:2106.00053 \[hep-ph\]](#).
- [106] D. Maurin *et al.*, *Phys. Rept.* **1161**, 1 (2026), [arXiv:2503.16173 \[astro-ph.HE\]](#).